Chemical Science

ROYAL SOCIETY OF CHEMISTRY

EDGE ARTICLE

View Article Online
View Journal | View Issue

Cite this: *Chem. Sci.*, 2025, **16**, 3259

All publication charges for this article have been paid for by the Royal Society of Chemistry

Fluorinated and methylated *ortho*-benzodipyrrole-based acceptors suppressing charge recombination and minimizing energy loss in organic photovoltaics†

Yan-Bo Wang,[a] Chia-Lin Tsai,[a] Yung-Jing Xue,[a] Bing-Huang Jiang,[b] Han-Cheng Lu,[a] Jun-Cheng Hong,[a] Yu-Chi Huang,[a] Kuo-Hsiu Huang,[a] Su-Ying Chien,[c] Chih-Ping Chen [b] and Yen-Ju Cheng *[ad]

The elimination of the A′ unit from A-$D_NA'_ND$-A-type Y6-derivatives has led to the development of a new class of *ortho*-benzodipyrrole (*o*-BDP)-based A-D_NB_ND-A-type NFAs. In this work, two new A-D_NB_ND-A-type NFAs, denoted as CFB and CMB, are designed and synthesized, where electron-withdrawing fluorine atoms and electron-donating methyl groups are substituted on the benzene ring of the *o*-BDP moiety, respectively. CFB exhibits a blue-shifted absorption spectrum, stronger intermolecular interactions, shorter π–π stacking distances, and more ordered 3D intermolecular packing in the neat and blend films, enabling it to effectively suppress charge recombination in the PM6:CFB device showing a higher PCE of 16.55% with an FF of 77.45%. CMB displays a higher HOMO/LUMO energy level, a smaller optical bandgap, and a less ordered 3D packing, which contributes to its superior ability to suppress energy loss in the PM6:CMB device with a high V_{oc} of 0.90 V and a PCE of 16.46%. To leverage the advantages of CFB and CMB, ternary PM6:Y6-16:CFB and PM6:Y6-16:CMB devices are fabricated. The PM6:Y6-16:CFB device exhibits the highest PCE of 17.83% with an increased V_{oc} of 0.86 V and a J_{sc} of 27.32 mA cm^{-2}, while the PM6:Y6-16:CMB device displayed an elevated V_{oc} of 0.87 V and an improved FF of 74.71%, leading to a PCE of 17.44%. The high PCE was achieved using the non-halogenated greener solvent *o*-xylene, highlighting their potential for facilitating more eco-friendly processing procedures. C-shaped disubstituted *o*-BDP-based A–D–A type acceptors open up new avenues for tailoring electronic properties and molecular self-assembly, achieving higher OPV performance with enhanced charge recombination suppression and reduced energy loss.

Received 21st October 2024
Accepted 8th January 2025

DOI: 10.1039/d4sc07146h

rsc.li/chemical-science

Introduction

Renowned for their flexibility, solution processability and transparency, organic solar cells have received considerable research interest in the realm of photovoltaics. In 2019, Y6 achieved a PCE of 15.7% when blended with donor polymer PM6,[1] ushering in a new era for organic non-fullerene acceptors (NFAs). Y6 features a unique structural arrangement characterized as A-$D_NA'_ND$-A in which the central heptacyclic ladder $D_NA'_ND$ π-core comprises an *ortho*-benzodipyrrole core laterally fused with two β-alkylated-thieno[3,2-*b*]thiophene moieties (TT, denoted as D) and vertically fused with an electron-deficient thiadiazole unit (Tz, denoted as A′). The label A usually corresponds to the 2-(5,6-difluoro-3-oxo-2,3-dihydro-1*H*-inden-1-ylidene)malononitrile (FIC) end-group acceptor, which is linked to the $D_NA'_ND$ core through olefination. Over the past five years, modifications of the A-$D_NA'_ND$-A architecture to fine-tune the photovoltaic properties have become the central focus of design and synthesis of organic NFA materials (Fig. 1). One strategy involves modifying the aliphatic side chains R_1 at nitrogen atoms[2–6] and R_2 at the β-position of thienothiophene (TT) units.[7–11] This approach has been primarily employed to tailor intermolecular interactions and adjust molecular packing within the material. On the other hand, conjugated main-chain engineering of the D units[12,13] and the A end-group acceptors[14–20] has been utilized to specifically modulate the intrinsic optical

[a]*Department of Applied Chemistry, National Yang Ming Chiao Tung University, 1001 University Road, Hsinchu, 30010, Taiwan*
[b]*Department of Materials Engineering and Organic Electronics Research Center, Ming Chi University of Technology, New Taipei City 24301, Taiwan*
[c]*Instrumentation Center, National Taiwan University, No. 1, Sec. 4, Roosevelt Road, Taipei 10617, Taiwan*
[d]*Center for Emergent Functional Matter Science, National Yang Ming Chiao Tung University, 1001 University Road, Hsinchu, 30010, Taiwan. E-mail: yjcheng@nycu.edu.tw*

† Electronic supplementary information (ESI) available. CCDC 2391682 and 2391712. For ESI and crystallographic data in CIF or other electronic format see DOI: https://doi.org/10.1039/d4sc07146h

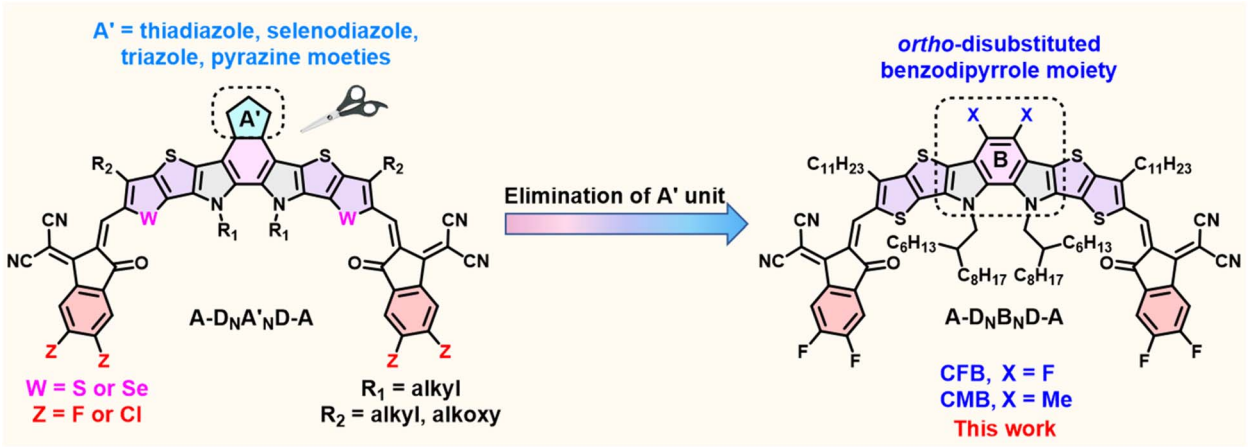

Fig. 1 Modification strategies for A-D_NB_ND-A type NFAs.

and electronic properties. For instance, replacing sulfur with selenium in the D units[12] or replacing fluorine with chlorine in the FIC units[7,14,20] causes a red-shift in absorption spectra and concomitantly enhances intermolecular interactions due to the presence of heavy atoms with higher polarizability. Another main-chain modification of the $D_NA'_ND$ core involves substituting Tz in the A′ unit with five-membered heterocycles such as triazole,[21–24] selenadiazole,[25,26] or six-membered pyrazine[27–31] and quinoxaline moieties.[32–36]

However, synthesis of $D_NA'_ND$ where the A′ unit is different from Tz is not straightforward. Cadogan cyclization, a key step in the formation of the benzodipyrrole moiety in $D_NA'_ND$, cannot be directly carried out in the presence of most heterocyclic A′ moieties. Instead, it usually involves reductive ring-opening of the thiadiazole unit in $D_NA'_ND$ to form a diamino species followed by the respective annulation.[37] Therefore, removing the A′ moiety from the A-$D_NA'_ND$-A structure can largely reduce synthetic complexity. Additionally, the impact of different heterocycle electron-deficient A′ units on the optical band-gaps associated with HOMO/LUMO energy levels and molecular self-assembly packing has not been well understood. To clarify the merits of the heterocycle-based A′ unit, we recently developed a new NFA, referred to as CB16,[38] which exhibits a structure identical to Y6, except for the elimination of the Tz moiety. CB16 can be structurally symbolized as A-D_NB_ND-A where C and B letters stands for C-shaped geometry and the central benzene ring, respectively. It was found that even without the Tz (A′) unit, CB16-based inverted OPVs can achieve comparable efficiencies to Y6 derivatives (Fig. 1). This research has unveiled that the central *ortho*-benzobipyrrole moiety that leads to a C-shaped geometry of A-D_NB_ND-A in CB16 and A-$D_NA'_ND$-A in Y6-based derivatives is pivotal in establishing the 3D molecular packing network for efficient charge transport, ultimately contributing to the superior performance of the devices. The heterocyclic A′ moiety plays a secondary role in finely adjusting intermolecular interactions, both internally within the NFA and externally with the polymer matrix. The further molecular engineering of the A-D_NB_ND-A structure holds significant potential for the development of a new generation of high-performance A–D–A-type CB-based NFAs.[39] Removal of the aromatic thiadiazole (Tz) group from A-$D_NA'_ND$-A simultaneously exposes two unsubstituted sp^2-carbons in the central benzene. Introducing non-aromatic substituents at the two active positions expands the scope of CB-series materials, thereby opening up avenues for new main-chain engineering to tailor their molecular properties. Through the introduction of electron-accepting and electron-releasing substitutions at the *o*-BDP moiety, it becomes feasible to systematically elucidate the electronic and steric effects of central substitutions on the molecular properties of A-D_NB_ND-A NFAs and their device performances. In this research, we designed and synthesized two new *ortho*-disubstituted A-D_NB_ND-A-type NFAs, denoted as CFB and CMB, which exhibit a C-shaped backbone similar to Y6-16, while incorporating fluorine and methyl groups onto the central benzene ring of the *o*-BDP moiety, respectively. Investigating the substitution effects of CMB and CFB helps clarify how the electron-accepting strength of A′ units (thiadiazole, selenadiazole, pyrazine, and triazole) in A-$D_NA'_ND$-A correlates with their absorption maxima and HOMO energy levels. Compared to the PM6:Y6-16 (the derivative of Y6 which has a 2-hexyldecyl side chain on the nitrogen of pyrrole) device with a PCE of 16.30%, the PM6:CFB device exhibited a higher PCE of 16.55% with an increased V_{oc} of 0.89 V and an improved FF of 77.15%, while the PM6:CMB device displayed an elevated V_{oc} of 0.90 V and an improved J_{sc} of 26.32 mA cm^{-2}, leading to a comparable PCE of 16.46%. By incorporating CFB and CMB as the second acceptor into the PM6: Y6-16 system, the ternary PM6:Y6-16:CFB and PM6:Y6-16:CMB devices demonstrated higher performances of 17.83% and 17.44%, respectively. Notably, the devices were fabricated using the greener solvent *o*-xylene, which addresses the toxicity concerns associated with halogenated solvents.[40–43]

Results and discussion

Molecular synthesis and thermal properties

The synthetic routes of *o*-BDP-based CFB and CMB are depicted in Scheme 1. Compound **1a** and **1b** were synthesized following

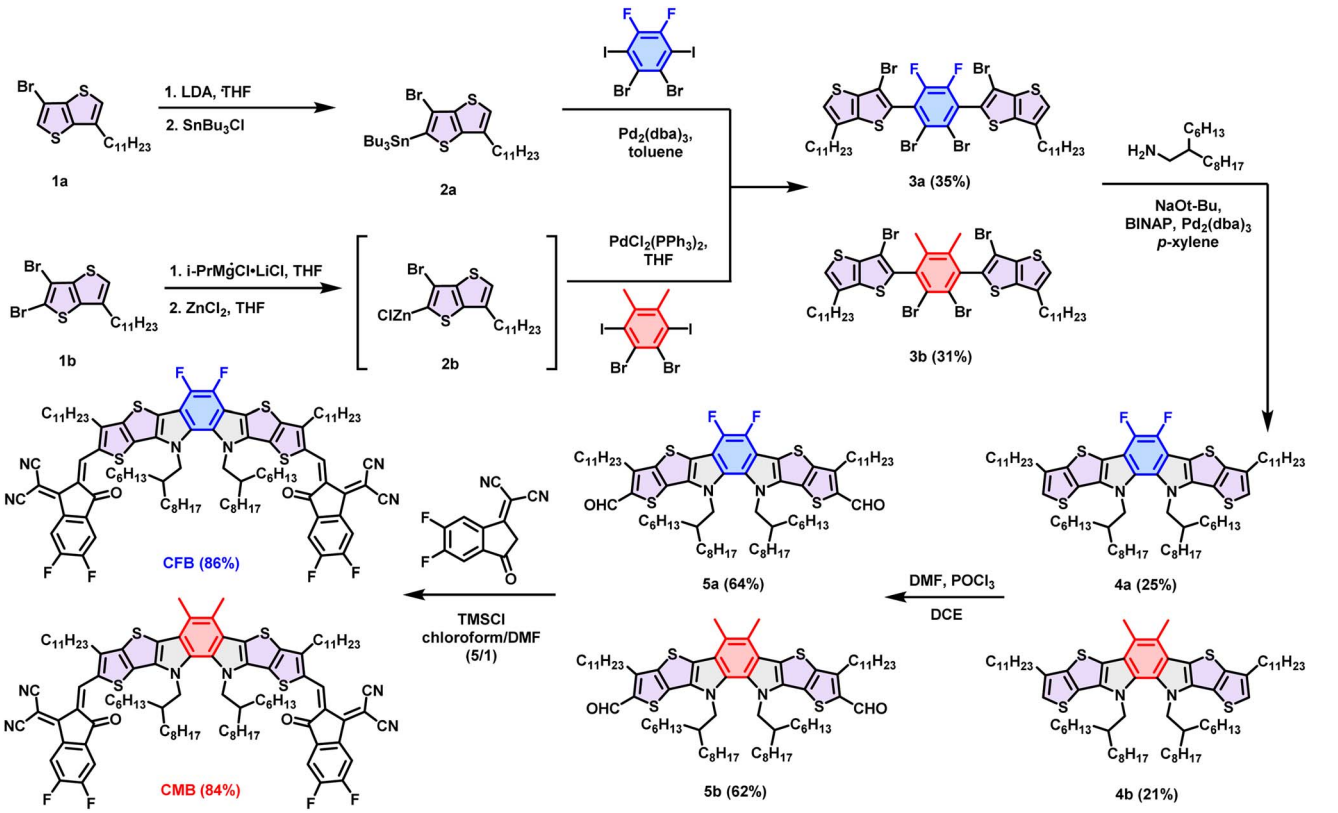

Scheme 1 Synthetic routes for *o*-BDP-based CFB and CMB.

procedures described in the literature.[38,44] Lithiation of compound **1a** by using lithium diisopropylamide (LDA) followed by treating with tributyltin chloride formed compound **2a**, which was further reacted with 1,2-dibromo-4,5-difluoro-3,6-diiodobenzene through Stille coupling to yield compound **3a**. Grignard metathesis of compound **1b** followed by quenching with $ZnCl_2$ resulted in intermediate **2b**. The Negishi coupling reaction of the freshly prepared **2b** with 1,2-dibromo-3,6-diiodo-4,5-dimethylbenzene afforded compound **3b**. Cyclization through multiple C–N bond formation achieved by Buchwald–Hartwig amination of **3a** and **3b** with 2-hexyldecyl amine led to the formation of **4a** and **4b**, respectively. Formylation through the Vilsmeier reaction of **4a** and **4b** yielded compound **5a** and **5b**, respectively. Knoevenagel condensation of **5a** or **5b** with FIC unit furnished two desired acceptors, CFB and CMB, with yields of 81% and 84%, respectively.

Thermogravimetric analysis (TGA) and differential scanning calorimetry (DSC) were conducted to assess thermal properties of the acceptors (Fig. S1† and 2a). While the decomposition temperature (T_d) of CMB resembles that of Y6-16 at 322 °C, the T_d of CFB increases to 330 °C, manifesting that the replacement of the Tz group with F atoms enhances thermal stability of the acceptors. In spite of the higher T_d, CFB exhibits a lower melting temperature (T_m) of 224 °C compared with Y6-16 (235 °C), indicating the weaker intermolecular interactions resulting from the removal of the central Tz unit. CMB has the smallest T_m of 222 °C, suggesting the least intermolecular interaction of the material.

Electrochemical and optical properties

Cyclic voltammetry was employed to determine the HOMO/LUMO energy levels of CFB and CMB (Fig. S2†), and the resulting energy level diagrams are depicted in Fig. 2b. In comparison with Y6-16, CFB featuring the electron-withdrawing F atoms exhibits a downshifted HOMO energy level of −5.85 eV and a similar LUMO energy level of −4.01 eV, resulting in an enlarged bandgap. Conversely, CMB containing electron-donating methyl groups shows upshifted HOMO/LUMO levels at −5.69/−3.96 eV, which is advantageous for increasing the V_{oc} value.

The absorption characteristics of typical A–D–A-type NFAs are primarily governed by push–pull photo-induced intramolecular charge transfer (ICT) from the electron-rich multi-fused D to the electron-withdrawing A moiety. However, the effect of various fused heterocyclic A′ units on the optical properties of A-D_NA′$_N$D-A-type Y-series NFAs has not been fully elucidated. The substitution at the central benzene ring of the A-$D_N$$B_N$D-A system can provide valuable insight to address this question. The absorption spectra are displayed in Fig. 2c with the features summarized in Table 1. Compared to Y6-16 with an absorption maximum (λ_{max}) at 734 nm in chloroform, CFB with two fluorine atoms exhibited a much blue-shifted λ_{max} at 704 nm, whereas CMB with two methyl groups showed a more red-shifted λ_{max} at 758 nm. The electron-accepting fluorine atoms positioned *para* to the two nitrogen atoms weaken their electron-donating ability through the inductive effect, which, in turn, reduces the ICT from the $D_N$$B_N$D to the A moieties.

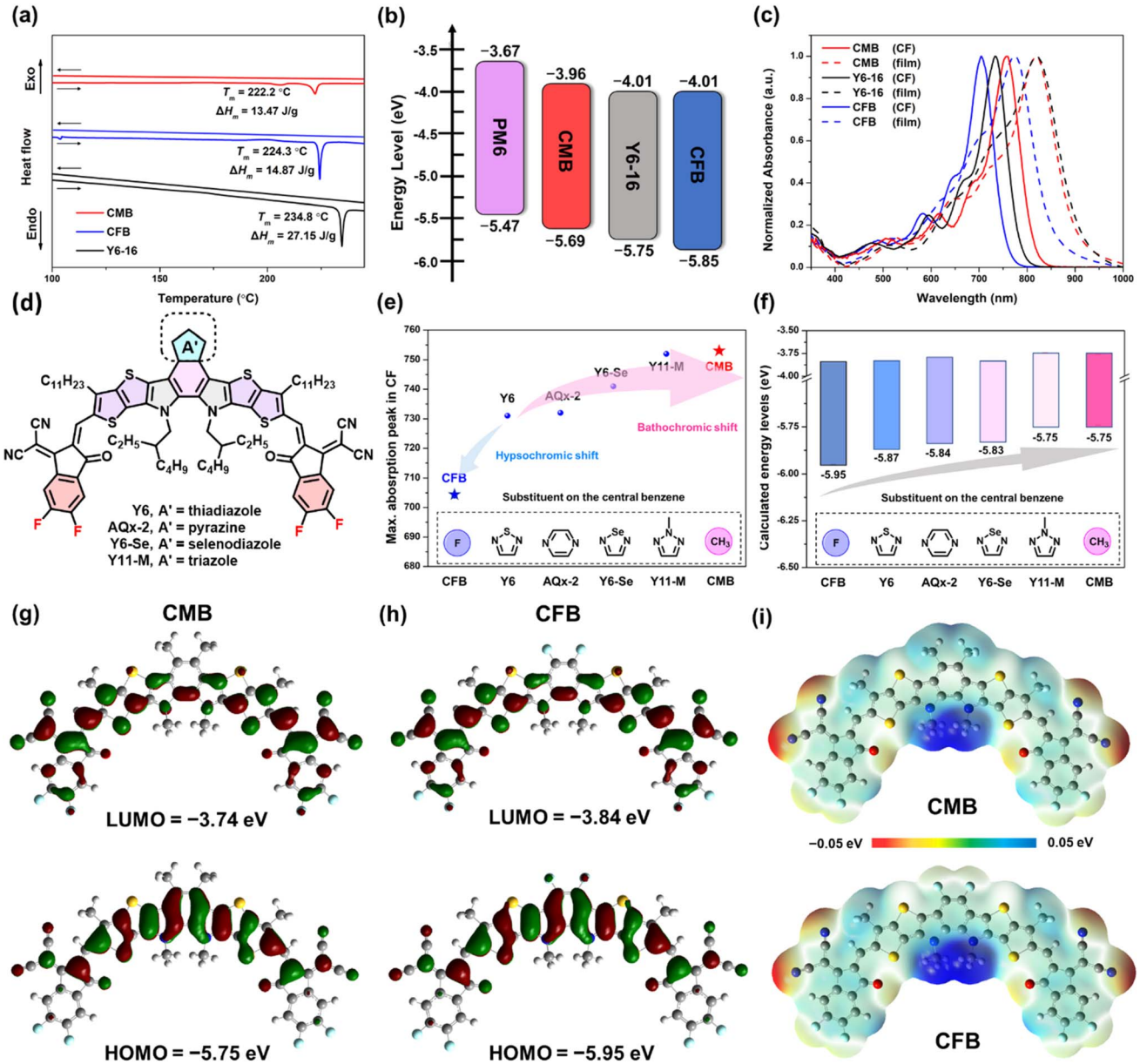

Fig. 2 (a) DSC measurements of CMB, Y6-16 and CFB with a ramping rate of 10 °C min^{-1}. (b) Energy levels diagram of PM6, CMB, Y6-16 and CFB estimated by cyclic voltammetry. (c) Normalized absorption spectra of CMB, Y6-16 and CFB in chloroform and thin films. (d) General structure of Y6, AQx-2, Y6-Se and Y11-M. (e) Absorption λ_{max} of *o*-BDP-based NFAs in chloroform. (f) Trend of the calculated HOMO level of *o*-BDP-based NFAs. HOMO/LUMO distribution of (g) CMB and (h) CFB. (i) Electrostatic potential distribution diagram of CMB and CFB.

Conversely, the moderately electron-donating methyl groups enhance the donating ability of the D_NB_ND unit, thereby augmenting the ICT effect.

Combining the A-D_NB_ND-A-type CFB and CMB with four other A-$D_NA'_ND$-A derivatives (Y6-16, AQx-2, Y6-Se, and Y11-M) reported in the literature, the solution λ_{max} values can be used

Table 1 Summary of optical and electrochemical properties of CMB, Y6-16 and CFB

NFA	Extinction coefficient[a] [$\times 10^5$ cm^{-1} M^{-1}]	λ_{max} [nm] Solu	Film	$\Delta\lambda$ [nm]	λ_{onset}[b] [nm]	$^cE_g^{opt}$ [eV]	HOMO[d] [eV]	LUMO[d] [eV]	$^dE_g^{ele}$ [eV]
Y6-16	1.86	734	819	85	911	1.36	−5.75	−4.01	1.74
CMB	1.51	758	820	62	902	1.37	−5.69	−3.96	1.73
CFB	1.80	704	774	70	858	1.45	−5.85	−4.01	1.84

[a] Calculated at λ_{max} in the solution state. [b] Calculated in the solid state. [c] $E_g^{opt} = 1240/\lambda_{onset}$. [d] Determined by cyclic voltammetry.

to quantify the electron-accepting ability of their respective A′ units (thiadiazole, pyrazine, selenodiazole, and triazole, depicted in Fig. 2d). The gradually increasing λ_{max} values for CFB (704 nm), Y6-16 (731 nm), AQx-2 (732 nm), Y6-Se (741 nm), Y11-M (753 nm), and CMB (758 nm) suggest that the electron-accepting ability of the A′ units follows this trend: difluoro > thiadiazole > pyrazine > selenodiazole > triazole > dimethyl.

This result provides a guideline for tuning the absorption properties of *o*-BDP-based NFAs by selecting substitutions on the central benzene ring (Fig. 2e). In addition, the λ_{max} of CFB is red-shifted to 774 nm ($\Delta\lambda_{max} = 70$ nm) from the solution state to the film state. The smaller $\Delta\lambda_{max}$ of CFB compared to that of Y6-16 ($\Delta\lambda_{max} = 85$ nm) indicates that the aromatic Tz unit induces stronger intermolecular interactions than F atoms. The λ_{max} of CMB in the film state is almost the same as that of Y6-16, leading to the smallest $\Delta\lambda_{max}$ ($\Delta\lambda_{max} = 62$ nm) among the three acceptors. The relatively larger steric hindrance of the methyl groups in CMB might further attenuate the intermolecular interactions.

Computational studies of frontier molecular orbitals

Energy level diagrams and frontier molecular orbitals of CFB and CMB along with Y6-16, AQx-1, Y6-Se, and Y11-M were calculated at the B3LYP/6-311G(d,p) level of theory, as shown in Fig. 2f–h and S3.† Substitution on the benzene ring of the D_NB_ND core has a more pronounced effect on the HOMO energy level than the LUMO energy level. Compared to Y6-16, which has HOMO/LUMO levels at −5.87 eV and −3.84 eV, respectively, CFB exhibits a more downshifted HOMO energy at −5.95 eV while maintaining an unchanged LUMO level at −3.84 eV. This suggests that the fluorine atoms in CFB exert a stronger electron-withdrawing effect than the Tz group in Y6-16. In both Y6-16 and CFB, the electron density in the HOMO is more dispersed into the fluorine atoms and the Tz group, while this effect is less evident in the LUMO. Additionally, the electron-donating dimethyl groups in CMB result in higher-lying HOMO/LUMO energy levels, at −5.75 eV and −3.74 eV, respectively. The theoretical trends in these energy levels are consistent with experimental results obtained from CV measurements. Overall, the calculated HOMO energy levels show a gradual upshift from −5.95 eV (CFB), −5.87 eV (Y6-16), −5.84 eV (AQx-2), −5.83 eV (Y6-Se), and −5.75 eV (Y11-M), to −5.75 eV (CMB), again reflecting the trend in electron-accepting ability: difluoro > thiadiazole > pyrazine > selenodiazole > triazole > dimethyl, as shown in Fig. 2f.

The calculated dipole moments (Fig. S4†) of CMB, Y6-16, and CFB were −3.448, 0.136, and 1.299, respectively. The negative dipole of CMB indicates that the dipole is oriented toward the substituent on the central benzene ring, suggesting a relatively positive charge due to its electron-donating ability. The larger positive dipole moment of CFB indicates a stronger electron-withdrawing core compared to Y6-16, which is consistent with the results observed in the absorption spectrum. CFB and CMB display similar molecular electrostatic potential (ESP) distributions, as shown in Fig. 2i. Most regions of the molecular surface exhibit positive ESP values, revealing the electron-accepting characteristics of both NFAs.

Molecular packing in single crystals

To elucidate the effect of substituting the Tz group with smaller substituents in the *o*-BDP core on molecular packing, single-crystal X-ray diffraction analysis was conducted. Single crystals of CFB and CMB were successfully acquired through vapor diffusion in acetonitrile and chloroform, and the crystallographic parameters for each crystal are provided in Table S1.† Data for single crystals of Y6-16 were extracted from the literature for comparison.[38] As depicted in Fig. 3a, CMB displays a relatively twisted central core with a θ value of 9.69° owing to the steric hindrance caused by the methyl groups, and also larger Φ values of 6.37° and 8.52°. In contrast, the torsion angle between two outer thiophene (θ) for CFB is 2.15° (Fig. 3b), which is smaller than that of Y6-16 (5.05°). Likewise, the dihedral angles (Φ) of CFB between the outer thiophene and terminal group for CFB are 1.38° and 4.53°, respectively, also much smaller than those of Y6-16 (4.67° and 8.55°). Overall, CFB exhibits a more planar structure than CMB.

Because of the C-shaped molecular geometry, both CMB and CFB molecules form a three-dimensional (3D) grid-like packing mode assembled *via* multiple π–π interactions (Fig. 3c and d). The π–π stacking distances in each mode are shown in Fig. 3e, f and S5.† CMB demonstrates five distinct dimeric π–π packing configurations (Fig. 3g) in a unit cell: the S-shaped TT-1 mode (TT, terminal to terminal), the U-shaped TT-2 mode, the M-shaped CT-1 mode (CT, core to terminal), the V-shaped CT-2 mode, and the Y-shaped CC–TT mode (CC, core to core). These configurations bear a resemblance to those observed in CB16,[38] indicating that the presence of dimethyl groups in CMB does not electronically alter the chemical environment. Consequently, the intermolecular interactions remain in a similar manner. The CC–TT mode, commonly observed in Y6 single crystals[45–47] associated with noncovalent S···N contacts between the Tz groups, has been theoretically shown to exhibit strong electronic coupling for both hole and electron transport.[34,47] Even though the central A′ group is eliminated, CMB also forms the CC–TT mode where the central *o*-xylene moieties are staggered to avoid the steric hindrance caused by the methyl groups, leading to an increased π–π distance of 3.57 Å between the two central molecules. In comparison to Y6-16, which exhibits 3D grid-like patterns containing a single type of elliptical void, CMB showcases more complex patterns featuring three distinct types of elliptical frames (Fig. 3c). The elliptical frames in CMB, measuring approximately 16.6 × 9.8 Å and 13.4 × 13.8 Å in size, are notably smaller than those observed in Y6-16, which are approximately 13.4 × 17.5 Å. The denser and more interpenetrating molecular arrangement in the CMB crystal provides an advantage for facilitating charge transport.

The unit cell in the crystal structure of CFB comprises four molecules forming only three distinct dimeric modes (Fig. 3f and h) including S-shape TT-1 mode, M-shape CC–TT mode and S-shape CT–CT mode. The core-to-core overlapping in the CC–TT mode within the CFB crystal is restricted to the terminal thiophene region, resulting in a larger π–π distance of 3.51 Å. On the other hand, compared to that of Y6-16, the CT–CT mode of CFB features a closer π–π distance of 3.38 Å and larger π–π

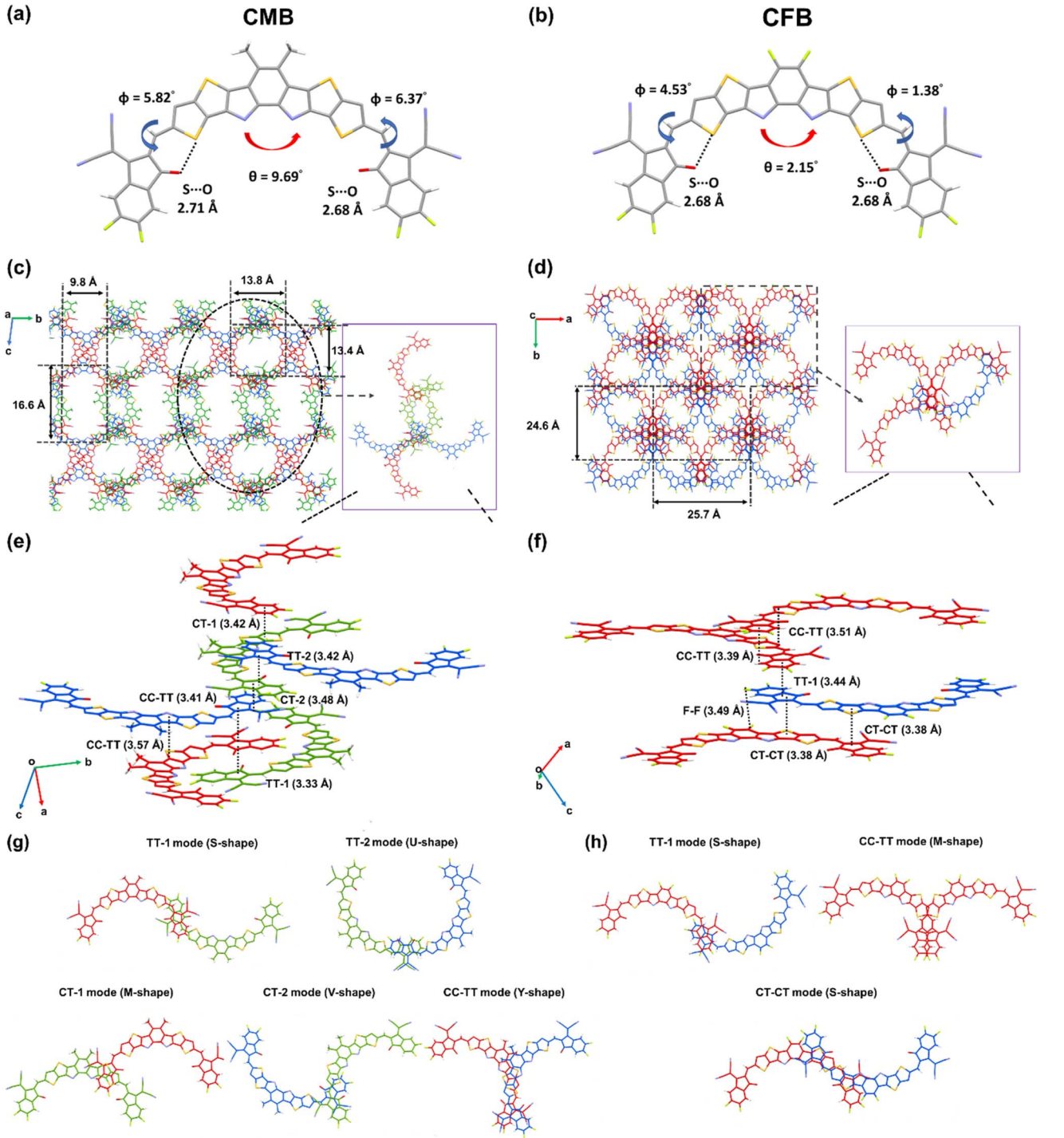

Fig. 3 The monomolecular crystallographic structure of (a) CMB and (b) CFB. 3D interpenetrating framework in single crystal of (c) CMB and (d) CFB projected from *a*- and *c*-crystallographic axes, respectively, with the insets illustrating the molecular packing in each unit cell; side views of the molecular packing with π−π distances corresponding to each distinct π−π packing mode found in one unit cell of (e) CMB and (f) CFB single crystals; five and three pairs of distinct π−π packing mode could be recognized in (g) CMB and (h) CFB, respectively. All the alkyl chains and H atoms are omitted to highlight the packing details. Three colors are used to discriminate between different conformers resulting from marginal variations in the twisted backbone.

overlapping. An additional F–F interaction, with a short contact distance of 3.49 Å, was observed between the *ortho*-difluorobenzene moiety (C) and the FIC acceptor (T) in the CTCT mode (Fig. 3f).

The CC–TT and CT–CT modes in CFB could offer more efficient charge transport channels.[33,34,47–50] Notably, the A-$D_NA'_ND$-A-type Y6-16 exhibits four dimeric packing modes. Compared to CMB (5 modes) and Y6-16 (4 modes), the decrease

in the number of packing modes found in CFB can be derived from the incorporation of compact difluoro atoms into the π-core structure to electronically manipulate the intermolecular interactions without imposing steric hindrance. The 3D packing framework of CFB reveals a circular void with dimensions of 24.6 × 25.7 Å (Fig. 3d). Viewed from the *c*-axis, the successive intersection of each circular ring with the other four gives rise to a highly organized kaleidoscope-like 3D structure, a feature previously unseen in any crystal structure within the Y6-series NFAs.[45–47] The intersecting regions within the circular frameworks are predominantly composed of FIC end-group acceptors, which form electron-transport channels along the end-group stacking. These results demonstrated that C-shaped A-D_NB_ND-A-type derivatives are capable of forming ordered and 3D interpenetrating packing structures. The two substituents on the central benzene ring could electronically and sterically modulate the packing configurations.

Device characteristics

OPV devices with an inverted architecture of ITO/ZnO/active layer/MoO_3/Ag were fabricated. PM6 was chosen as the p-type polymer to blend with the three acceptors with an optimal weight ratio of 1 : 1.2 in wt%. The active layers were prepared by spin-coating PM6:NFA solutions using *o*-xylene as the greener solvent without any additive. The standard PM6:Y6-16-based device showed a J_{sc} of 26.37 mA cm^{-2}, an FF of 74.48% and a V_{oc} of 0.83 V with a PCE of 16.30%. CFB with two electron-withdrawing fluorine atoms shows a significantly blue-shifted absorption compared to Y6-16. Consequently, the PM6:CFB device delivered a relatively lower J_{sc} of 24.00 mA cm^{-2}. However, it showed a higher FF of 77.45% and an improved V_{oc} of 0.89 V, leading to a better PCE of 16.55%. This suggests a reduction in energy loss for the CFB-based device, given the identical LUMO energy level between CFB and Y6-16. It should also be noted that the integrated J_{sc} extracted from the EQE spectrum of the PM6:CFB device is larger than that of PM6:Y6-16 before 850 nm, indicating that the former exhibits superior charge dynamics within its own absorption region. The PM6:CFB blend is likely to exhibit a more favorable morphology for efficient charge transport. As evidenced by its single-crystal structure, CFB with fluorine atoms may promote better alignment and packing of the molecules within the active layer, facilitating more effective electron transport pathways. Additionally, the interaction between CFB and the PM6 polymer matrix may lead to improved interfacial properties, enhancing charge extraction efficiency and reducing charge recombination.

CMB featuring electron-donating methyl groups enhances absorption capability and upshifts the LUMO energy level. Consequently, the PM6:CMB-based device achieved a J_{sc} of 26.32 mA cm^{-2} and the highest V_{oc} of 0.90 V, leading to a comparable PCE of 16.46%. However, the FF of 69.50% is only moderate, presumably due to the steric hindrance of the dimethyl groups that cause inferior molecular packing of CMB within the blend. Considering that the PM6:CFB device has a higher V_{oc}, and a higher integrated EQE J_{sc} before 840 nm, we introduced CFB into the PM6:Y6-16 blend as a second acceptor in an attempt to increase V_{oc} and to complement the absorption range with Y6-16. By combining the absorption/EQE strength of CFB in 500–800 nm and Y6-16 in 800–950 nm, the ternary PM6:Y6-16:CFB (1 : 0.6 : 0.6 in wt%) device achieved a largely improved J_{sc} of 27.32 mA cm^{-2} along with an improved V_{oc} of 0.86 V, delivering a superior PCE of 17.83% that surpasses those of both the binary PM6:Y6-16 and PM6-CFB devices. By a similar strategy, through the introduction of Y6-16 to modulate the intermolecular packing in the PM6:CMB blend, the ternary PM6:Y6-16:CMB (1 : 0.6 : 0.6 in wt%) device exhibited a much improved FF of 74.71% with a high V_{oc} of 0.87 V, and a slightly enhanced J_{sc} of 26.76 mA cm^{-2}, achieving a PCE of 17.44% that also outperforms both the binary PM6:Y6-16 and PM6-CMB devices. The *J*–*V* curves and EQE spectra of the optimized devices are shown in Fig. 4a–c with device parameters summarized in Tables 2 and S2–S5.†

Charge dynamics analysis

To understand the charge recombination behaviors, the dependence of light intensity on J_{sc} and V_{oc} was investigated and illustrated in Fig. 4d and e. According to the formula $J_{sc} \propto (P_{light})^{\alpha}$, the slope of the natural logarithm of light intensity *versus* J_{sc} yields the exponential factor α, which would be close to 1 if bimolecular recombination is effectively suppressed.[51,52] The relationship of V_{oc} and P_{light} followed the rule $V_{oc} \propto n(kT/q)\ln(P_{light})$ and represented the possibility of trap-assisted recombination.[53] The α and n values are close to 1 for all the devices (α = 0.936, 0.971, 0.977; n = 1.14, 1.11, 1.06 for PM6:CMB, PM6:Y6-16 and PM6:CFB, respectively), indicating a relatively low degree of bimolecular recombination and trap-assisted recombination in the devices. Though having similar absorption spectra, Y6-16 based devices showed better suppression of both types of recombination compared to the CMB-based devices, leading to a slightly higher J_{sc} and FF. The CFB-based devices possessed the lowest degree of recombination, coinciding with the highest FF, again suggesting that the relatively lower J_{sc} should mainly be attributed to the blue-shifted absorption.

To investigate the charge dissociation and charge collection properties, the relationship of photocurrent density (J_{ph}) *versus* effective voltage (V_{eff}) was evaluated.[54] The ratio of J_{sc} to saturated current density (J_{sat}) yields exciton dissociation efficiency (P_{diss}) while the ratio of J_{max} to saturated current density (J_{sat}) indicates charge collection efficiency (P_{coll}). As depicted in Fig. 4f, the CFB-based device possessed the highest value of 88.33% for P_{coll}, which may be partially attributed to the better film morphology and higher FF. Although the CMB-based device has a P_{diss} value similar to that of the Y6-16 based device, it shows a lower P_{coll}, indicating that the slightly lower J_{sc} is likely due to morphological issues rather than differences in charge generation properties.

Transient photocurrent (TPC) and transient photovoltage (TPV) measurements were conducted to gain insight into the charge carrier dynamics for the OPVs. As shown in Fig. 4g, the shortest charge extraction time of 0.34 μs, extracted by the exponential decay fitting of TPC data,[55] was observed for PM6:CFB based devices (compared to 0.39 μs and 0.37 μs for

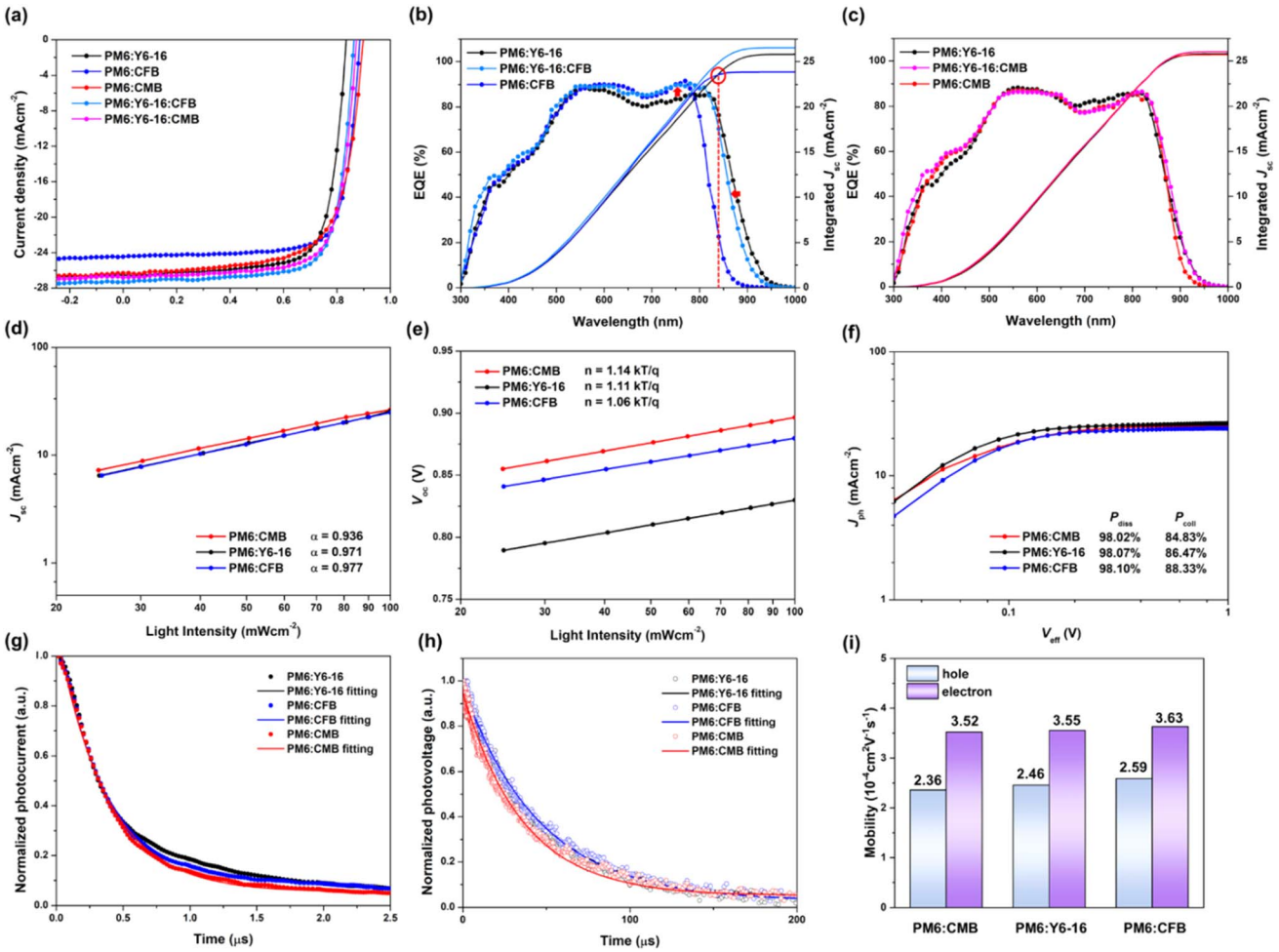

Fig. 4 (a) *J*–*V* curves of PM6:Y6-16, PM6:CFB, PM6:CMB, PM6:Y6-16:CFB and PM6:Y6-16:CMB devices. EQE spectrum of (b) CFB-based devices and (c) CMB-based devices. (d) J_{sc} *versus* light intensity, (e) V_{oc} *versus* light intensity and (f) J_{ph} *versus* V_{eff} spectra for the PM6:CMB, PM6:Y6-16 and PM6:CFB devices. (g) Transient photocurrent curves (dots) and corresponding fitting curves (solid lines) and (h) transient photovoltage curves (circles) and corresponding fitting curves (solid lines) for the optimized binary devices. (i) SCLC electron and hole mobilities of the optimized binary devices.

PM6:Y6-16 and PM6:CMB-based devices), suggesting better charge extraction ability. Meanwhile, the longest carrier lifetime of 46.2 μs for the PM6:CFB-based device was extracted from TPV measurements (compared to 44.4 μs and 36.7 μs for PM6:Y6-16 and PM6:CMB-based devices), indicating the lowest charge recombination probability for this blend (Fig. 4h). The combination of more efficient charge extraction and the prolonged carrier lifetime simultaneously contributes to the highest P_{coll} and well-suppressed charge recombination behaviors observed in the PM6:CFB-based device. It should be noted that the shorter charge carrier lifetime for PM6:CMB based devices may explain their relatively larger recombination probability.

Moreover, space-charge-limited current (SCLC) measurements were also conducted using both hole-only and electron-only devices to evaluate charge transport properties.[56] The calculated hole/electron mobilities are $2.59 \times 10^{-4}/3.63 \times 10^{-4}$, $2.46 \times 10^{-4}/3.55 \times 10^{-4}$ and $2.36 \times 10^{-4}/3.52 \times 10^{-4}$ $cm^2\ V^{-1}\ s^{-1}$ for PM6:CFB, PM6:Y6-16 and PM6:CMB devices, respectively (Fig. 4i). The CFB device exhibits the highest mobilities and the most balanced electron-to-hole mobility ratio μ_e/μ_h of 1.40,

Table 2 Optimized device parameters for the binary and ternary OPVs

Active layer	Blend ratio in wt%	V_{oc} [V]	J_{sc} [mA cm^{-2}]	FF [%]	PCE [%]
PM6:Y6-16	1 : 1.2	0.83 (0.83 ± 0.01)	26.37 (26.46 ± 0.66)	74.48 (73.62 ± 1.44)	16.30 (16.17 ± 0.15)
PM6:CFB	1 : 1.2	0.89 (0.89 ± 0.01)	24.00 (24.14 ± 0.28)	77.45 (76.39 ± 0.94)	16.55 (16.35 ± 0.23)
PM6:CMB	1 : 1.2	0.90 (0.89 ± 0.01)	26.32 (25.97 ± 0.62)	69.50 (70.35 ± 1.69)	16.46 (16.33 ± 0.05)
PM6:Y6-16:CFB	1 : 0.6 : 0.6	0.86 (0.867 ± 0.004)	27.32 (27.00 ± 0.20)	75.61 (75.01 ± 1.03)	17.83 (17.57 ± 0.19)
PM6:Y6-16:CMB	1 : 0.6 : 0.6	0.87 (0.875 ± 0.002)	26.76 (26.53 ± 0.16)	74.71 (74.04 ± 0.56)	17.44 (17.20 ± 0.14)

which corresponds to the highest PCE value. These findings suggest that incorporating small withdrawing F groups is an effective strategy for reducing charge recombination losses.

For the ternary devices, the charge dynamics analysis is shown in Fig. S6, S7 and Table S6.† Introduction of CFB into the PM6:Y6-16 device resulted in α and n values approaching 1, an extended charge carrier lifetime of over 60 μs, increased P_{coll}, and higher mobilities, contributing to a high J_{sc} above 27 mA cm^{-2}. Likewise, the ternary PM6:Y6-16:CMB device also demonstrated enhanced parameters, suggesting that incorporating CMB into the PM6:Y6-16 device also effectively reduces charge recombination.

Energy loss analysis

To investigate the significant improvement in V_{oc} observed in both CFB- and CMB-based devices compared to Y6-16, the total energy loss (E_{loss}) of the OPVs, defined by using the equation $E_{loss} = E_g - qV_{oc}$, was analyzed. The bandgap (E_g) values were estimated from the cross-point of the normalized FTPS-EQE and electroluminescence (EL) spectra,[57,58] yielding values of 1.425, 1.482, and 1.420 for the PM6:Y6-16, PM6:CFB, and PM6:CMB devices, respectively. Total E_{loss} is determined to be 0.598, 0.593, and 0.522 eV for PM6:Y6-16, PM6:CFB, and PM6:CMB devices, respectively. Although both the CFB and CMB-based devices exhibited lower E_{loss} compared to the Y6-16 based device, the reasons for the V_{oc} improvement are different. The higher V_{oc} of the CFB-based device can be attributed to both the larger bandgap and reduced E_{loss}, while the increased V_{oc} of the CMB-based device was solely due to the reduction in E_{loss} because the E_g values of CMB and Y6-16 are the same. Since V_{oc} is determined by two factors ($qV_{oc} = E_g - E_{loss}$), the plot of E_{loss}/E_g values for the devices, shown in Fig. 5a, intuitively reflects the

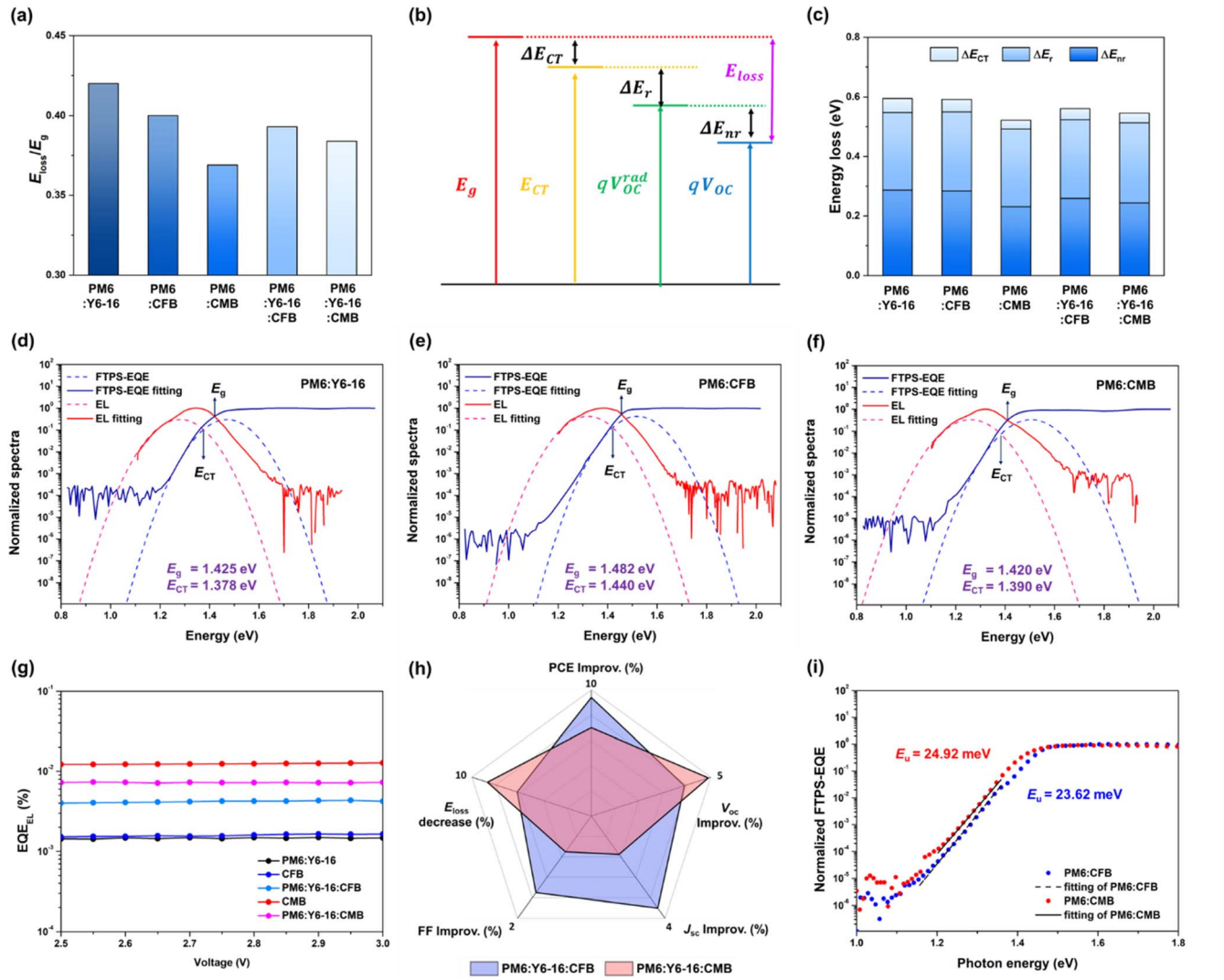

Fig. 5 (a) Statistical diagram of the ratio of E_{loss} to E_g. (b) Schematic diagram of E_{loss} related parameters. (c) Statistical diagram of E_{loss} decomposed into three ΔE_{CT}, ΔE_r and ΔE_{nr} terms. The cross-point of normalized FTPS-EQE and EL spectra of (d) PM6:Y6-16, (e) PM6:CFB, and (f) PM6:CMB blend films is used to determine the E_g value. The fitting curves are depicted as dashed lines, and the cross-point of the fitting curves is used to determine the E_{CT} value. (g) EQE_{EL} spectra for all the optimized devices. (h) Radar diagram of the OPV parameter percentage improvement and E_{loss} percentage decrease in the ternary devices compared with the PM6:Y6-16 based devices. (i) Normalized FTPS-EQE spectra with exponential fitting results of the PM6:CFB and PM6:CMB blend films.

Table 3 Detailed parameters of energy loss analysis of the binary and ternary OPVs

Active layer	E_g[a] [eV]	V_{oc} [V]	E_{CT}[b] [eV]	ΔE_{CT}[c] [eV]	ΔE_r[d] [V]	ΔE_{nr}[e] [V]	EQE_{EL}	E_{loss} [eV]	E_u[f] [meV]
PM6:Y6-16	1.425	0.827	1.378	0.047	0.261	0.287	1.46×10^{-5}	0.598	24.39
PM6:CFB	1.482	0.889	1.440	0.042	0.266	0.284	1.58×10^{-5}	0.593	23.62
PM6:CMB	1.420	0.898	1.390	0.030	0.261	0.231	1.24×10^{-5}	0.522	24.92
PM6:Y6-16:CFB	1.428	0.867	1.391	0.037	0.265	0.259	4.19×10^{-5}	0.561	23.94
PM6:Y6-16:CMB	1.421	0.875	1.388	0.033	0.269	0.244	7.25×10^{-5}	0.546	24.04

[a] Bandgap was estimated from the cross-point of normalized FTPS-EQE and EL spectra. [b] E_{CT} was obtained from the fitting curves of normalized FTPS-EQE and EL spectra. [c] ΔE_{CT} was determined from the equation $\Delta E_{CT} = E_g - E_{CT}$. [d] ΔE_r was determined from the equation $\Delta E_r = E_{CT}/q\text{-}V_{oc} - \Delta E_{nr}$. [e] ΔE_{nr} was determined from EQE_{EL} results, which followed the equation $\Delta E_{nr} = (kT/q)\ln(1/EQE_{EL})$. [f] E_u was obtained by exponential fitting of the low-energy part of the FTPS-EQE spectra.

magnitude of V_{oc}. The smaller E_{loss}/E_g values of 0.37 and 0.40 for the PM6:CMB and PM6:CFB devices correspond to higher V_{oc} values of 0.90 and 0.89 V, compared to PM6: Y6-16 (E_{loss}/E_g = 0.40, V_{oc} = 0.83 V). The total E_{loss} can be further divided into three components ($E_{loss} = \Delta E_{CT} + \Delta E_r + \Delta E_{nr}$, Fig. 5b), as detailed in Table 3 and Fig. 5c: charge generation loss (ΔE_{CT}), radiative charge recombination (ΔE_r), and non-radiative charge recombination (ΔE_{nr}).[58–61] ΔE_{CT} is the difference between E_g and E_{CT} (charge transfer state) which can be estimated by fitting normalized FTPS-EQE and EL spectra,[55,62,63] as depicted in Fig. 5d–f and S8.† It should be noted that the PM6:CFB and PM6:CMB devices exhibited higher-lying E_{CT} compared to the PM6:Y6-16 device, which resulted in reduced ΔE_{CT}. This suggests a potential hybridization of the LE (localized excited) and CT states[64,65] and a further suppression of electron coupling between the lowest CT state and the highest vibrational ground state,[66] which is one of the contributions to ΔE_{nr}.[66,67] ΔE_{nr} was experimentally obtained from EQE_{EL} spectra (Fig. 5g) using the equation $\Delta E_{nr} = (kT/q)\ln(1/EQE_{EL})$,[68] resulting in values of 0.284 and 0.231 for the PM6:CFB and PM6:CMB-based devices, respectively, which are smaller than the 0.287 observed for the PM6:Y6-16-based device.

In the ternary devices, incorporating CFB and CMB into the binary PM6:Y6-16 blend reduces ΔE_{nr} to 0.259 eV and 0.244 eV, and total E_{loss} to 0.561 eV and 0.546 eV, respectively, with the latter having a more significant effect, leading to much improved V_{oc} values of 0.86 V and 0.87 V compared to the binary PM6:Y6-16 device (V_{oc} = 0.83 V). Fig. 5h displays a radar diagram illustrating the percentage improvements in OPV parameters and the decrease in E_{loss} for the ternary PM6:Y6-16:CFB and PM6:Y6-16:CMB devices compared to the reference PM6:Y6-16-based device. The diagram clearly reveals that CMB with electron-donating methyl groups significantly suppress E_{loss} and thus enhance V_{oc} due to its electronic effects, whereas CFB, with electron-donating fluorine atoms, primarily optimizes intermolecular packing, leading to improved J_{sc} and FF.

Device film morphology analysis

To elucidate the packing features of the neat NFA films as well as blend films with PM6, grazing incidence wide-angle X-ray scattering (GIWAXS) experiments were carried out at the 25A1 coherent X-ray scattering beamline of the Taiwan Photon Source (TPS). The 2D diffraction patterns as well as their corresponding 1D line-cut profiles in the in-plane (q_{xy}) and out-of-plane (q_z) directions are depicted in Fig. 6. As illustrated in Fig. 6a, all the neat films exhibited a strong (010) diffraction peak in the q_z direction, suggesting the preference of face-on orientations of the NFAs.

Y6-16 exhibited a diffraction at $q_z = 1.79$ Å^{-1} corresponding to the smallest π–π stacking distance (d_π) of 3.51 Å due to the additional molecular interactions induced by the thiadiazole group. CFB and CMB showed diffractions at $q_z = 1.77$ Å^{-1} and 1.75 Å^{-1} corresponding to the larger π–π stacking distance of 3.55 Å and 3.59 Å, respectively, suggesting that molecular interactions in the neat films follow the trend Y6-16 > CFB > CMB, which is consistent with the trend observed in $\Delta\lambda_{max}$ in the absorption spectra. Furthermore, the crystalline coherence lengths (CCL, L_c) of π–π stacking ($L_{c\ \pi\text{–}\pi}$) in the neat films, derived from the full width at half maximum (FWHM) and listed in Table 4, show a gradual increase from 14.50 Å for CMB, to 17.14 Å for CFB, and further to 17.67 Å for Y6-16. The GIWAXS patterns of PM6:Y6-16, PM6:CFB and PM6:CMB blend films exhibited similar face-on oriented π–π stacking reflection centered at 1.77 Å^{-1}, 1.76 Å^{-1} and 1.74 Å^{-1}, corresponding to a gradually increased d_π of 3.55 Å, 3.57 Å and 3.61 Å, respectively. In comparison to the as-cast neat films, the blend films exhibit a slight increase in the d_π due to the interpenetration of NFAs within the PM6 matrix, and the trend of the π–π stacking distance in the blend films aligns with that observed in the neat films. Besides, all the blend films showed a distinct (100) diffraction peak at q_{xy} ~0.30 Å^{-1} corresponding to the lamellar side-chain packing of PM6 (Fig. 6b and c).

It is noteworthy that the $L_{c\ \pi\text{–}\pi}$ of the PM6:CFB film reaches the highest value of 23.56 Å attributed to the more ordered packing benefited from the fluorine atoms. We also determined the Urbach energy (E_u) by performing an exponential fit on the low photon energy region of the normalized FTPS-EQE spectra. The results are provided in Table 3 and illustrated in Fig. 5i and S9.† The smallest E_u value of 23.62 meV observed in the PM6:CFB device suggests a higher degree of molecular order, which is consistent with its largest $L_{c\ \pi\text{–}\pi}$ value.[25,33,34,69,70]

In the ternary devices (Fig. 6d), the introduction of CFB into the PM6:Y6-16 film led to an increase in L_c in both the q_{xy} and q_z directions, suggesting that CFB promotes higher crystallinity within the blend, improving film morphology and enhancing charge transport dynamics.[11] Similarly, the addition of CMB to the PM6:Y6-16 film demonstrated a similar effect, implying that CMB also interacts well with both PM6 and Y6-16 in the ternary system. However, the increased π–π stacking distance to 3.59 Å indicates that the steric effect of the central dimethyl groups persists which

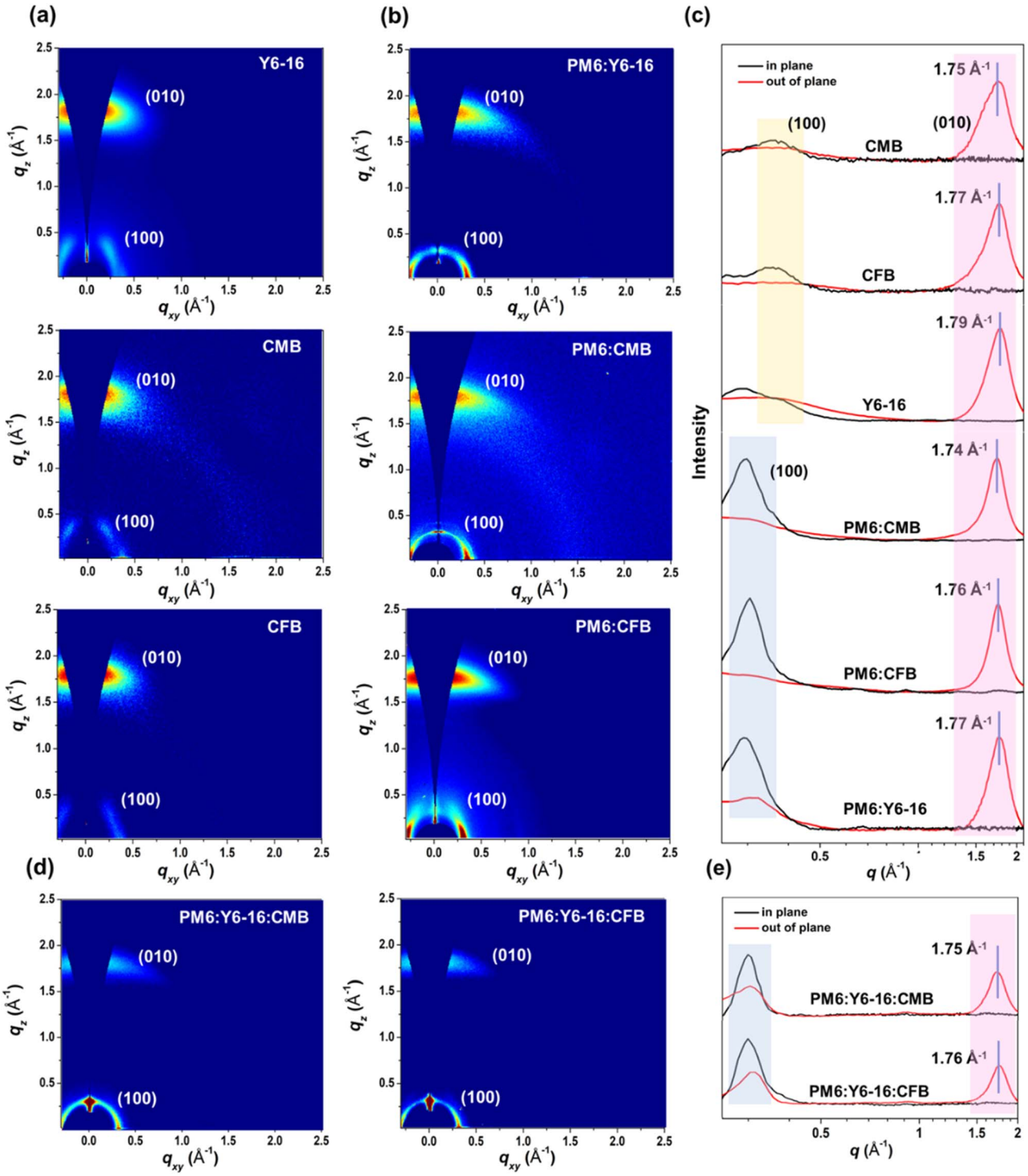

Fig. 6 (a) 2D GIWAXS patterns of neat Y6-16, CMB and CFB films. (b) 2D GIWAXS patterns of PM6:Y6-16, PM6:CMB and PM6:CFB blend films. (c) The corresponding 1D profiles along the in-plane and out-of-plane direction. (d) 2D GIWAXS patterns of the ternary films. (e) Corresponding 1D profiles of the ternary films along the in-plane and out-of-plane direction.

may partly explain the slightly lower FF observed in the PM6:Y6-16:CMB device compared to the PM6:Y6-16:CFB device.

Atomic force microscopy (AFM) was also used to examine the morphology of the neat and blend films. As depicted in Fig. 7, both Y6-16 and CFB neat films showed a very smooth surface and root-meant-square (RMS) roughness of around 1 nm. Despite the similar RMS in neat films, the PM6:CFB film possessed a much smoother surface (RMS = 1.48 nm) with a much clearer interpenetrating fibrillar structure than that of the PM6:Y6-16 film (RMS = 2.19 nm), indicating the better interaction between CFB and PM6. As for CMB, both the neat and blend films have a relatively rougher RMS of 1.61 and 2.68

Table 4 The structural parameters deduced from GIWAXS patterns of the neat NFA films as well as their blend films with PM6. The parameters q_z and q_{xy} indicated the peak center in the in-plane and out-of-plane direction, respectively, and their corresponding d-spacing, d_π, was also listed. The crystal coherence length, L_c, was derived from the full-width at half-maximum (FWHM) δq using the Scherrer equation with a shape factor of 0.9

	In-plane reflection peak				Out-of-plane reflection peak			
Film	q_{xy} [Å^{-1}]	d_l [Å]	δq_{xy} [Å^{-1}]	L_C [Å]	q_z [Å^{-1}]	d_π [Å]	δq_z [Å^{-1}]	L_C [Å]
CMB	0.37	16.98	0.14	40.39	1.75	3.59	0.39	14.50
CFB	0.36	17.45	0.15	37.70	1.77	3.55	0.33	17.14
Y6-16	0.36	17.45	0.19	29.76	1.79	3.51	0.32	17.67
PM6:CMB	0.30	20.94	0.08	70.69	1.74	3.61	0.30	18.85
PM6:CFB	0.30	20.94	0.07	80.78	1.76	3.57	0.24	23.56
PM6:Y6-16	0.29	21.67	0.07	80.78	1.77	3.55	0.26	21.75
PM6:Y6-16:CMB	0.30	20.94	0.05	113.10	1.75	3.59	0.255	22.17
PM6:Y6-16:CFB	0.30	20.94	0.06	94.24	1.76	3.57	0.250	22.62

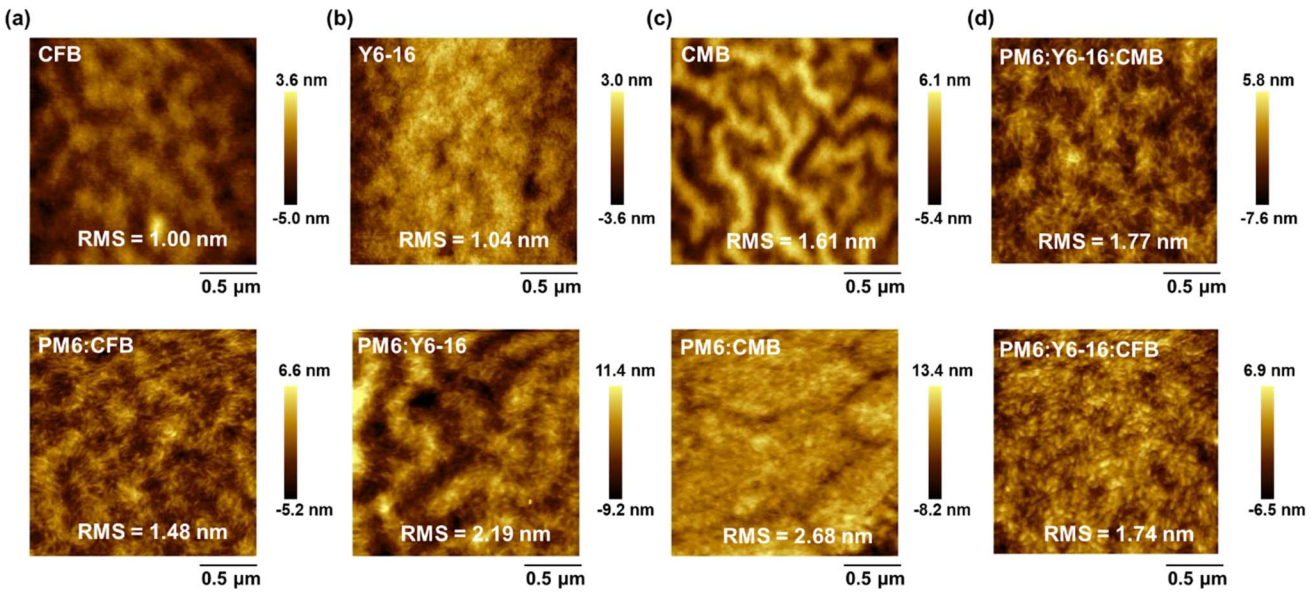

Fig. 7 AFM height images of (a) CFB and PM6:CFB, (b) Y6-16 and PM6:Y6-16, (c) CMB and PM6:CMB and (d) ternary blend films.

nm, respectively, compared with the other two acceptors. However, with the largest RMS, the PM6:CMB film still presented a fibrillar structure, which may partially account for the comparable performance with the PM6:Y6-16 device. It should be noted that the introduction of CFB into the PM6:Y6-16 blend led to a dramatic decrease in roughness (RMS = 1.67 nm, Fig. 7d) and the appearance of a much clearer and more delicate fibrillar network structure.[28,38] This suggests that CFB may enhance interactions in the PM6:Y6-16:CFB blend, contributing to the high FF and improved performance. A similar phenomenon was observed after introducing CMB into the PM6:Y6-16 blend (Fig. 7d), indicating that CMB also interacts effectively with both PM6 and Y6-16 in this system.

Contact angle measurements of the neat films of the NFAs and PM6 were conducted to obtain the Flory–Huggins interaction parameter (χ), which was used to evaluate the miscibility between donor–acceptor and acceptor–acceptor pairs (Fig. S10 and Table S7†). The χ values between PM6 and CFB, Y6-16, and CMB are 0.24, 0.35, and 0.55, respectively. The gradually increasing χ values suggest a decrease in miscibility between the donor and acceptor, which correlates well with the fill factor (FF) results. Moreover, the small χ value between Y6-16 and either CFB or CMB indicates good miscibility between the NFAs and explains the improved FF in the ternary system. Considering all morphological analyses, we can infer that the disubstituted C-shaped *o*-BDP skeletons of CFB and CMB play a crucial role in their effective interactions with both PM6 and Y6-16 in the ternary system, contributing to the significant improvement in PCE for the ternary devices.

Conclusions

Elimination of the A′ unit in Y6-series A-$D_NA'_ND$-A type structures enables the introduction of two new non-aromatic substitutions on the central *o*-benzodipyrrole core, while preserving its C-shaped molecular skeleton. In this work, we designed and synthesized two CB-based A-D_NB_ND-A-type architecture NFAs, CFB and CMB, by introducing two F atoms and methyl groups on the central benzene ring, respectively. The electron-withdrawing F

atoms in CFB reduce the electron-donating strength of the *o*-BDP unit and weaken the ICT effect, leading to a larger bandgap, a blue-shifted absorption spectrum and a downshifted HOMO energy level. Conversely, the electron-donating methyl groups in CMB result in upshifted HOMO/LUMO energy levels, a narrower band gap and a red-shifted absorption spectrum compared to those of Y6-16. The high electronegativity and compactness of F atoms facilitate intermolecular interactions without sterically affecting molecular self-assembly, leading to a highly ordered kaleidoscope-like 3D packing network with shorter π–π stacking distances in the single crystal structure. These characteristics reduce charge recombination, enhance charge mobilities and elongate carrier lifetime in the devices. In contrast, CMB forms a more complicated 3D structure with five dimeric π–π stacking modes due to the steric effect of the dimethyl *o*-BDP moiety.

Compared to the PM6:Y6-16 device, the binary PM6:CFB device exhibited a higher V_{oc} of 0.89 V, the highest FF of 77.45% but a lower J_{sc} of 24 mA cm^{-2}, whereas the binary PM6:CMB device exhibited the highest V_{oc} of 0.90 V, a J_{sc} of 26.32 mA cm^{-2} but a lower FF of 69.50%. To leverage the advantages of both CFB and CMB, the ternary PM6:Y6-16:CFB and PM6:Y6-16:CMB devices were fabricated and optimized. With CFB's excellent charge generation, transport, and collection properties, along with its highly ordered packing and well-defined fibrillar structure when blended with PM6, the ternary PM6:Y6-16:CFB device showed a significant increase in J_{sc} to 27.32 mA cm^{-2}, coupled with a moderate improvement in V_{oc} to 0.86 V, resulting in the highest PCE of 17.83% in comparison with the standard PM6:Y6-16 device. CMB demonstrates a superior ability to suppress E_{loss}, particularly by reducing ΔE_{nr}. Consequently, the PM6:Y6-16:CMB device effectively improved the V_{oc} to 0.87 V, along with a moderate enhancement in J_{sc}, yielding a PCE of 17.44%. The enhanced performance of the ternary devices suggests that the disubstituted *o*-BDP skeleton in both CFB and CMB plays a key role in forming a compatible morphology with both PM6 and Y6-16, thereby maximizing device parameters. Furthermore, the use of a greener nonhalogenated solvent for device fabrication underscores the potential for eco-friendly processing procedures to mitigate toxicity concerns. Substituting the central benzene ring of these C-shaped *o*-BDP-based A–D–A type NFAs provides valuable insights into the structure–property relationship and offers new avenues for tailoring intrinsic properties and molecular self-assembly that can achieve higher OPV performance with reduced charge recombination and energy loss.

Data availability

The data supporting the findings of this study are available within the article and ESI.† The X-ray crystallographic coordinates for structures of CMB and CFB have been deposited at the Cambridge Crystallographic Data Centre (CCDC) with 2391712 and 2391682.

Author contributions

The project was conceived and conceptualized by Yen-Ju Cheng and Yan-Bo Wang. Yan-Bo Wang, Yung-Jing Xue, Jun-Cheng Hong, and Kuo-Hsiu Huang synthesized the compounds and carried out measurements of their optical and electrochemical properties, and GIWAXS analysis. The fabrication and characterization of the OPVs were performed by Yan-Bo Wang, Chia-Lin Tsai, Bing-Huang Jiang, Han-Cheng Lu, Yu-Chi Huang, and Chih-Ping Chen. Su-Ying Chien conducted single-crystal X-ray crystallography. The manuscript was drafted by Yan-Bo Wang and Yen-Ju Cheng.

Conflicts of interest

There are no conflicts to declare.

Acknowledgements

This work was supported by the National Science and Technology Council, Taiwan (grant no. 112-2221-E-A49-002 and 113-2113-M-A49-015-MY3) and Ministry of Education, Taiwan (SPROUT Project-Center for Emergent Functional Matter Science of National Yang Ming Chiao Tung University). We thank the National Center of High-Performance Computing (NCHC) in Taiwan for computer time and facilities. GIWAXS measurement support from TPS 25 beamlines of the National Synchrotron Radiation Research Center (NSRRC) is acknowledged; special thank goes to Dr Yi-Wei Tsai for help in the GIWAXS data processing.

Notes and references

1 J. Yuan, Y. Zhang, L. Zhou, G. Zhang, H.-L. Yip, T.-K. Lau, X. Lu, C. Zhu, H. Peng and P. A. Johnson, Single-junction organic solar cell with over 15% efficiency using fused-ring acceptor with electron-deficient core, *Joule*, 2019, **3**, 1140–1151.

2 K. Jiang, Q. Wei, J. Y. L. Lai, Z. Peng, H. K. Kim, J. Yuan, L. Ye, H. Ade, Y. Zou and H. Yan, Alkyl chain tuning of small molecule acceptors for efficient organic solar cells, *Joule*, 2019, **3**, 3020–3033.

3 Z. Abbas, S. U. Ryu, M. Haris, C. E. Song, H. K. Lee, S. K. Lee, W. S. Shin, T. Park and J.-C. Lee, Optimized vertical phase separation via systematic Y6 inner side-chain modulation for non-halogen solvent processed inverted organic solar cells, *Nano Energy*, 2022, **101**, 107574.

4 M. Deng, X. Xu, Y. Duan, L. Yu, R. Li and Q. Peng, Y-type non-fullerene acceptors with outer branched side chains and inner cyclohexane side chains for 19.36% efficiency polymer solar cells, *Adv. Mater.*, 2023, **35**, 2210760.

5 C. Kim, J. H. Lee, J. S. Park, S. Lee, T. N.-L. Phan, Y.-H. Kim and B. J. Kim, Impact of the molecular structure of oligo (ethylene glycol)-incorporated Y-series acceptors on the formation of alloy-like acceptors and performance of non-halogenated solvent-processable organic solar cells, *ACS Appl. Mater. Interfaces*, 2023, **15**, 24670–24680.

6 G. U. Kim, C. Sun, D. Lee, G. S. Choi, J. S. Park, S. Seo, S. Lee, D. Y. Choi, S. K. Kwon and S. Cho, Effect of the selective halogenation of small molecule acceptors on the blend

morphology and voltage loss of high-performance solar cells, *Adv. Funct. Mater.*, 2022, **32**, 2201150.

7 Y. Cui, H. Yao, J. Zhang, K. Xian, T. Zhang, L. Hong, Y. Wang, Y. Xu, K. Ma and C. An, Single-junction organic photovoltaic cells with approaching 18% efficiency, *Adv. Mater.*, 2020, **32**, 1908205.

8 Y. Chang, J. Zhang, Y. Chen, G. Chai, X. Xu, L. Yu, R. Ma, H. Yu, T. Liu and P. Liu, Achieving efficient ternary organic solar cells using structurally similar non-fullerene acceptors with varying flanking side chains, *Adv. Energy Mater.*, 2021, **11**, 2100079.

9 G. Chai, Y. Chang, J. Zhang, X. Xu, L. Yu, X. Zou, X. Li, Y. Chen, S. Luo and B. Liu, Fine-tuning of side-chain orientations on nonfullerene acceptors enables organic solar cells with 17.7% efficiency, *Energy Environ. Sci.*, 2021, **14**, 3469–3479.

10 G. Chai, Y. Chang, Z. Peng, Y. Jia, X. Zou, D. Yu, H. Yu, Y. Chen, P. C. Chow and K. S. Wong, Enhanced hindrance from phenyl outer side chains on nonfullerene acceptor enables unprecedented simultaneous enhancement in organic solar cell performances with 16.7% efficiency, *Nano Energy*, 2020, **76**, 105087.

11 D. Jeong, G. U. Kim, D. Lee, S. Seo, S. Lee, D. Han, H. Park, B. Ma, S. Cho and B. J. Kim, Sequentially fluorinated polythiophene donors for high-performance organic solar cells with 16.4% efficiency, *Adv. Energy Mater.*, 2022, **12**, 2201603.

12 F. Lin, K. Jiang, W. Kaminsky, Z. Zhu and A. K.-Y. Jen, A non-fullerene acceptor with enhanced intermolecular π-core interaction for high-performance organic solar cells, *J. Am. Chem. Soc.*, 2020, **142**, 15246–15251.

13 H. Yu, Z. Qi, J. Zhang, Z. Wang, R. Sun, Y. Chang, H. Sun, W. Zhou, J. Min and H. Ade, Tailoring non-fullerene acceptors using selenium-incorporated heterocycles for organic solar cells with over 16% efficiency, *J. Mater. Chem. A*, 2020, **8**, 23756–23765.

14 Y. Cui, H. Yao, L. Hong, T. Zhang, Y. Tang, B. Lin, K. Xian, B. Gao, C. An and P. Bi, Organic photovoltaic cell with 17% efficiency and superior processability, *Natl. Sci. Rev.*, 2020, **7**, 1239–1246.

15 G. Li, X. Zhang, L. O. Jones, J. M. Alzola, S. Mukherjee, L.-w. Feng, W. Zhu, C. L. Stern, W. Huang and J. Yu, Systematic merging of nonfullerene acceptor π-extension and tetrafluorination strategies affords polymer solar cells with> 16% efficiency, *J. Am. Chem. Soc.*, 2021, **143**, 6123–6139.

16 Y. Shi, J. Pan, J. Yu, J. Zhang, F. Gao, K. Lu and Z. Wei, Optimizing the charge carrier and light management of nonfullerene acceptors for efficient organic solar cells with small nonradiative energy losses, *Sol. RRL*, 2021, **5**, 2100008.

17 D. Mo, H. Chen, J. Zhou, L. Han, Y. Zhu, P. Chao, N. Zheng, Z. Xie and F. He, Isomeric effects of chlorinated end groups on efficient solar conversion, *J. Mater. Chem. A*, 2020, **8**, 23955–23964.

18 H. Wang, L. Han, J. Zhou, T. Liu, D. Mo, H. Chen, H. Lai, N. Zheng, Z. Xie and W. Zheng, Isomerism: minor changes in the bromine substituent positioning lead to notable differences in photovoltaic performance, *CCS Chem.*, 2021, **3**, 2591–2601.

19 Z. Luo, R. Ma, Z. Chen, Y. Xiao, G. Zhang, T. Liu, R. Sun, Q. Zhan, Y. Zou and C. Zhong, Altering the positions of chlorine and bromine substitution on the end group enables high-performance acceptor and efficient organic solar cells, *Adv. Energy Mater.*, 2020, **10**, 2002649.

20 C. He, Z. Chen, T. Wang, Z. Shen, Y. Li, J. Zhou, J. Yu, H. Fang, Y. Li and S. Li, Asymmetric electron acceptor enables highly luminescent organic solar cells with certified efficiency over 18, *Nat. Commun.*, 2022, **13**, 2598.

21 S. Liu, J. Yuan, W. Deng, M. Luo, Y. Xie, Q. Liang, Y. Zou, Z. He, H. Wu and Y. Cao, High-efficiency organic solar cells with low non-radiative recombination loss and low energetic disorder, *Nat. Photonics*, 2020, **14**, 300–305.

22 Z. Li, C. Zhu, J. Yuan, L. Zhou, W. Liu, X. Xia, J. Hong, H. Chen, Q. Wei and X. Lu, Optimizing side chains on different nitrogen aromatic rings achieving 17% efficiency for organic photovoltaics, *J. Energy Chem.*, 2022, **65**, 173–178.

23 F. Qi, K. Jiang, F. Lin, Z. Wu, H. Zhang, W. Gao, Y. Li, Z. Cai, H. Y. Woo and Z. Zhu, Over 17% efficiency binary organic solar cells with photoresponses reaching 1000 nm enabled by selenophene-fused nonfullerene acceptors, *ACS Energy Lett.*, 2020, **6**, 9–15.

24 Y. Cho, Z. Sun, K. M. Lee, G. Zeng, S. Jeong, S. Yang, J. E. Lee, B. Lee, S.-H. Kang and Y. Li, CF3-terminated side chain enables efficiencies surpassing 18.2% and 16.1% in small- and large-scale manufacturing of organic solar cells, *ACS Energy Lett.*, 2022, **8**, 96–106.

25 Z. Zhang, Y. Li, G. Cai, Y. Zhang, X. Lu and Y. Lin, Selenium heterocyclic electron acceptor with small urbach energy for as-cast high-performance organic solar cells, *J. Am. Chem. Soc.*, 2020, **142**, 18741–18745.

26 W. Gao, F. Qi, Z. Peng, F. R. Lin, K. Jiang, C. Zhong, W. Kaminsky, Z. Guan, C. S. Lee and T. J. Marks, Achieving 19% power conversion efficiency in planar-mixed heterojunction organic solar cells using a pseudosymmetric electron acceptor, *Adv. Mater.*, 2022, **34**, 2202089.

27 Z. Zhou, W. Liu, G. Zhou, M. Zhang, D. Qian, J. Zhang, S. Chen, S. Xu, C. Yang and F. Gao, Subtle molecular tailoring induces significant morphology optimization enabling over 16% efficiency organic solar cells with efficient charge generation, *Adv. Mater.*, 2020, **32**, 1906324.

28 M. Xie, Y. Shi, L. Zhu, J. Zhang, Q. Cheng, H. Zhang, Y. Yan, M. Zhu, H. Zhou and K. Lu, Selective halogenation of central and end-units of nonfullerene acceptors enables enhanced molecular packing and photovoltaic performance, *Energy Environ. Sci.*, 2023, **16**, 3543–3551.

29 Y. Ding, S. Xiong, M. Li, M. Pu, Y. Zhu, X. Lai, Y. Wang, D. Qiu, H. Lai and F. He, Highly-Efficient 2D Nonfullerene Acceptors Enabled by Subtle Molecular Tailoring Engineering, *Small*, 2023, 2309169.

30 Z. Chen, J. Ge, Y. Guo, M. Zhao, J. Shi, Y. Qiu, E. Zhou and Z. Ge, Modification on the quinoxaline unit to achieve high open-circuit voltage and morphology optimization for organic solar cells, *ACS Energy Lett.*, 2022, **7**, 3432–3438.

31 Y. Jiang, Y. Li, F. Liu, W. Wang, W. Su, W. Liu, S. Liu, W. Zhang, J. Hou and S. Xu, Suppressing electron-phonon coupling in organic photovoltaics for high-efficiency power conversion, *Nat. Commun.*, 2023, **14**, 5079.

32 H. Chen, H. Liang, Z. Guo, Y. Zhu, Z. Zhang, Z. Li, X. Cao, H. Wang, W. Feng and Y. Zou, Central unit fluorination of non-fullerene acceptors enables highly efficient organic solar cells with over 18% efficiency, *Angew. Chem.*, 2022, **134**, e202209580.

33 H. Liang, X. Bi, H. Chen, T. He, Y. Lin, Y. Zhang, K. Ma, W. Feng, Z. Ma and G. Long, A rare case of brominated small molecule acceptors for high-efficiency organic solar cells, *Nat. Commun.*, 2023, **14**, 4707.

34 Y. Zou, H. Chen, X. Bi, X. Xu, H. Wang, M. Lin, Z. Ma, M. Zhang, C. Li and X. Wan, Peripheral halogenation engineering controls molecular stacking to enable highly efficient organic solar cells, *Energy Environ. Sci.*, 2022, **15**, 3519–3533.

35 K. Liu, Y. Jiang, F. Liu, G. Ran, F. Huang, W. Wang, W. Zhang, C. Zhang, J. Hou and X. Zhu, Organic solar cells with over 19% efficiency enabled by a 2D-conjugated non-fullerene acceptor featuring favorable electronic and aggregation structures, *Adv. Mater.*, 2023, **35**, 2300363.

36 S. Oh, D. Jeong, K. Bae, G. U. Kim, T. N. L. Phan, J. W. Lee, J. Park, D. Lee, S. Cho and B. J. Kim, Impact of Linker Engineering in Core-Linked Dimeric Acceptors for High-Performance Organic Solar Cells, *Adv. Funct. Mater.*, 2024, **34**, 2406501.

37 Y.-J. Cheng, C.-H. Chen, Y.-J. Ho, S.-W. Chang, H. A. Witek and C.-S. Hsu, Thieno [3, 2-b] pyrrolo donor fused with benzothiadiazolo, benzoselenadiazolo and quinoxalino acceptors: synthesis, characterization, and molecular properties, *Org. Lett.*, 2011, **13**, 5484–5487.

38 Y.-J. Xue, Z.-Y. Lai, H.-C. Lu, J.-C. Hong, C.-L. Tsai, C.-L. Huang, K.-H. Huang, C.-F. Lu, Y.-Y. Lai and C.-S. Hsu, Unraveling the Structure–Property–Performance Relationships of Fused-Ring Nonfullerene Acceptors: Toward a C-Shaped ortho-Benzodipyrrole-Based Acceptor for Highly Efficient Organic Photovoltaics, *J. Am. Chem. Soc.*, 2023, **146**, 833–848.

39 H. Lai, Z. Deng and F. He, C-shaped ADA non-fullerene acceptor achieves efficient organic solar cells, *Joule*, 2024, **8**, 572–575.

40 M. Kim, S. U. Ryu, S. A. Park, Y.-J. Pu and T. Park, Designs and understanding of small molecule-based non-fullerene acceptors for realizing commercially viable organic photovoltaics, *Chem. Sci.*, 2021, **12**, 14004–14023.

41 Y. Yang, S. U. Ryu, F. Wu, H. Lu, K. Jia, C. Zhong, T. Park and L. Zhu, Blending isomers of fluorine-substituted sulfonyldibenzene as hole transport materials to achieve high efficiency beyond 21% in perovskite solar cells, *Chem. Eng. J.*, 2021, **424**, 130396.

42 C. Kim, S. Chen, J. S. Park, G.-U. Kim, H. Kang, S. Lee, T. N.-L. Phan, S.-K. Kwon, Y.-H. Kim and B. J. Kim, Green solvent-processed, high-performance organic solar cells achieved by outer side-chain selection of selenophene-incorporated Y-series acceptors, *J. Mater. Chem. A*, 2021, **9**, 24622–24630.

43 J. Lee, J. W. Kim, S. A. Park, S. Y. Son, K. Choi, W. Lee, M. Kim, J. Y. Kim and T. Park, Study of burn-in loss in green solvent-processed ternary blended organic photovoltaics derived from UV-crosslinkable semiconducting polymers and nonfullerene acceptors, *Adv. Energy Mater.*, 2019, **9**, 1901829.

44 J. H. Wan, W. F. Fang, Z. F. Li, X. Q. Xiao, Z. Xu, Y. Deng, L. H. Zhang, J. X. Jiang, H. Y. Qiu and L. B. Wu, Novel Ladder π-Conjugated Materials—Sila-Pentathienoacenes: Synthesis, Structure, and Electronic Properties, *Chem. Asian J.*, 2010, **5**, 2290–2296.

45 G. Zhang, X.-K. Chen, J. Xiao, P. C. Chow, M. Ren, G. Kupgan, X. Jiao, C. C. Chan, X. Du and R. Xia, Delocalization of exciton and electron wavefunction in non-fullerene acceptor molecules enables efficient organic solar cells, *Nat. Commun.*, 2020, **11**, 3943.

46 W. Zhu, A. P. Spencer, S. Mukherjee, J. M. Alzola, V. K. Sangwan, S. H. Amsterdam, S. M. Swick, L. O. Jones, M. C. Heiber and A. A. Herzing, Crystallography, morphology, electronic structure, and transport in non-fullerene/non-indacenodithienothiophene polymer: Y6 solar cells, *J. Am. Chem. Soc.*, 2020, **142**, 14532–14547.

47 G. Kupgan, X. Chen and J.-L. Bredas, Molecular packing of non-fullerene acceptors for organic solar cells: Distinctive local morphology in Y6 vs. ITIC derivatives, *Mater. Today Adv.*, 2021, **11**, 100154.

48 H. Lai, H. Chen, Z.-Y. Chen, Y. Lang, Y. Zhu, S.-T. Zhang, X. Lai, P. Tan, Y. Zhang and B. Yang, Exploring the significance of packing modes and 3D framework sizes and utilizing three chlorine-mediated acceptors and the "like dissolves like" approach for achieving an efficiency over 19, *Energy Environ. Sci.*, 2023, **16**, 5944–5955.

49 D. Yuk, M. H. Jee, C. W. Koh, W. W. Park, H. S. Ryu, D. Lee, S. Cho, S. Rasool, S. Park and O. H. Kwon, Simplified Y6-Based Nonfullerene Acceptors: In-Depth Study on Molecular Structure–Property Relation, Molecular Dynamics Simulation, and Charge Dynamics, *Small*, 2023, **19**, 2206547.

50 S. i. Kato, T. Furuya, M. Nitani, N. Hasebe, Y. Ie, Y. Aso, T. Yoshihara, S. Tobita and Y. Nakamura, A Series of π-Extended Thiadiazoles Fused with Electron-Donating Heteroaromatic Moieties: Synthesis, Properties, and Polymorphic Crystals, *Chem.–Eur. J.*, 2015, **21**, 3115–3128.

51 A. K. K. Kyaw, D. H. Wang, C. Luo, Y. Cao, T. Q. Nguyen, G. C. Bazan and A. J. Heeger, Effects of Solvent Additives on Morphology, Charge Generation, Transport, and Recombination in Solution-Processed Small-Molecule Solar Cells, *Adv. Energy Mater.*, 2014, **4**, 1301469.

52 P. Hartnagel and T. Kirchartz, Understanding the light-intensity dependence of the short-circuit current of organic solar cells, *Adv. Theory Simul.*, 2020, **3**, 2000116.

53 F. Gao, Z. Li, J. Wang, A. Rao, I. A. Howard, A. Abrusci, S. Massip, C. R. McNeill and N. C. Greenham, Trap-induced losses in hybrid photovoltaics, *ACS Nano*, 2014, **8**, 3213–3221.

54 V. Mihailetchi, J. Wildeman and P. W. Blom, Space-charge limited photocurrent, *Phys. Rev. Lett.*, 2005, **94**, 126602.
55 P. Bi, C. An, T. Zhang, Z. Chen, Y. Xu, Y. Cui, J. Wang, J. Li, Y. Wang and J. Ren, Achieving 31% efficiency in organic photovoltaic cells under indoor light using a low energetic disorder polymer donor, *J. Mater. Chem. A*, 2023, **11**, 983–991.
56 P. Murgatroyd, Theory of space-charge-limited current enhanced by Frenkel effect, *J. Phys. D: Appl. Phys.*, 1970, **3**, 151.
57 J. Wang, M. Zhang, J. Lin, Z. Zheng, L. Zhu, P. Bi, H. Liang, X. Guo, J. Wu and Y. Wang, An asymmetric wide-bandgap acceptor simultaneously enabling highly efficient single-junction and tandem organic solar cells, *Energy Environ. Sci.*, 2022, **15**, 1585–1593.
58 H. H. Chiu, B.-H. Jiang, H. C. Wang, X.-M. Su, Y.-H. Kang, Y.-W. Su, H.-S. Shih, C.-P. Chen and Y. J. Chang, Indolocarbazole-based small molecules as guest donors for High-Performance ternary organic photovoltaics, *Chem. Eng. J.*, 2023, **469**, 143938.
59 O. D. Miller, E. Yablonovitch and S. R. Kurtz, Strong internal and external luminescence as solar cells approach the Shockley–Queisser limit, *IEEE J. Photovoltaics*, 2012, **2**, 303–311.
60 N. An, Y. Cai, H. Wu, A. Tang, K. Zhang, X. Hao, Z. Ma, Q. Guo, H. S. Ryu and H. Y. Woo, Solution-processed organic solar cells with high open-circuit voltage of 1.3 V and low non-radiative voltage loss of 0.16 V, *Adv. Mater.*, 2020, **32**, 2002122.
61 Y. Xu, H. Yao, L. Ma, J. Wang and J. Hou, Efficient charge generation at low energy losses in organic solar cells: a key issues review, *Rep. Prog. Phys.*, 2020, **83**, 082601.
62 J. Wang, Y. Cui, Y. Xu, K. Xian, P. Bi, Z. Chen, K. Zhou, L. Ma, T. Zhang and Y. Yang, A new polymer donor enables binary all-polymer organic photovoltaic cells with 18% efficiency and excellent mechanical robustness, *Adv. Mater.*, 2022, **34**, 2205009.
63 K. Vandewal, K. Tvingstedt, A. Gadisa, O. Inganäs and J. V. Manca, Relating the open-circuit voltage to interface molecular properties of donor: acceptor bulk heterojunction solar cells, *Phys. Rev. B:Condens. Matter Mater. Phys.*, 2010, **81**, 125204.
64 X.-K. Chen, D. Qian, Y. Wang, T. Kirchartz, W. Tress, H. Yao, J. Yuan, M. Hülsbeck, M. Zhang and Y. Zou, A unified description of non-radiative voltage losses in organic solar cells, *Nat. Energy*, 2021, **6**, 799–806.
65 F. D. Eisner, M. Azzouzi, Z. Fei, X. Hou, T. D. Anthopoulos, T. J. S. Dennis, M. Heeney and J. Nelson, Hybridization of local exciton and charge-transfer states reduces nonradiative voltage losses in organic solar cells, *J. Am. Chem. Soc.*, 2019, **141**, 6362–6374.
66 J. Benduhn, K. Tvingstedt, F. Piersimoni, S. Ullbrich, Y. Fan, M. Tropiano, K. A. McGarry, O. Zeika, M. K. Riede and C. J. Douglas, Intrinsic non-radiative voltage losses in fullerene-based organic solar cells, *Nat. Energy*, 2017, **2**, 1–6.
67 D. He, F. Zhao, C. Wang and Y. Lin, Non-radiative recombination energy losses in non-fullerene organic solar cells, *Adv. Funct. Mater.*, 2022, **32**, 2111855.
68 S. Ullbrich, J. Benduhn, X. Jia, V. C. Nikolis, K. Tvingstedt, F. Piersimoni, S. Roland, Y. Liu, J. Wu and A. Fischer, Emissive and charge-generating donor–acceptor interfaces for organic optoelectronics with low voltage losses, *Nat. Mater.*, 2019, **18**, 459–464.
69 F. Urbach, The long-wavelength edge of photographic sensitivity and of the electronic absorption of solids, *Phys. Rev.*, 1953, **92**, 1324.
70 X. Ma, C. Tang, Y. Ma, X. Zhu, J. Wang, J. Gao, C. Xu, Y. Wang, J. Zhang and Q. Zheng, Over 17% efficiency of ternary organic photovoltaics employing two acceptors with an acceptor–donor–acceptor configuration, *ACS Appl. Mater. Interfaces*, 2021, **13**, 57684–57692.